Published in Nano Energy, doi.org/10.1016/j.nanoen.2023.109081, Vol. 119, 109081, 2024

Bandgap engineering of BZT-BCT by Mn doping and the emerging strong photo-pyroelectric effect

Lu Wang [a, b, ξ], Faqiang Zhang [c, ξ], Chen Chen [a], Xiang He [a], Muzaffar Ahmad Boda [a], Kui Yao [d, *], Zhiguo Yi [a, b, *]

[a] State Key Laboratory of High Performance Ceramics and Superfine Microstructure, Shanghai Institute of Ceramics, Chinese Academy of Sciences, Shanghai 200050, China

[b] Center of Materials Science and Optoelectronics Engineering, University of Chinese Academy of Sciences, Beijing 100049, China

[c] CAS Key Laboratory of Inorganic Functional Materials and Devices, Shanghai Institute of Ceramics, Chinese Academy of Sciences, Shanghai 200050, China

[d] Institution of Materials Research and Engineering, Agency for Science, Technology and Research (A*STAR), 138634, Singapore

[ξ] These authors contributed equally to this work.

* Corresponding author.

E-mail address: k-yao@imre.a-star.edu.sg (K. Yao), zhiguo@mail.sic.ac.cn (Z. Yi)

Developing narrow bandgap ferroelectrics with a sizable polarization presents great potential toward photoelectric applications. Unfortunately, most ferroelectrics exhibit wide bandgaps, while lowering their bandgaps constantly accompanies the serious deterioration of ferroelectricity. By utilizing the Jahn-Teller (J-T) effect of Mn ion, here we report an exception of lead-free ferroelectric $0.5Ba(Zr_{0.2-x}Ti_{0.8}Mn_x)$-$0.5(Ba_{0.7}Ca_{0.3})TiO_3$ ceramics showing narrow bandgaps and large polarizations. Especially for the composition x = 0.12, a low bandgap of 1.2 eV with a high residual polarization 9.9 μC/cm^2 is achieved. Further investigations indicate that it has negligible photovoltaic effect due to the high density of point

defects, but a significant improvement in near-infrared (NIR) light induced pyroelectric response, driven by the simultaneously increased photothermal conversion ability and room temperature pyroelectric coefficient. The pyroelectric device as demonstrated shows excellent linear dependence on the NIR light intensity with current and voltage sensitivities of 0.169 nA/(mW/cm^2) and 0.052 V/(mW/cm^2), respectively. Furthermore, the device possesses substantial pyroelectric response to the infrared irradiation from human body and excellent anti-interference ability. This study not only find an excellent lead-free ferroelectric composition for human body recognition, but also provide a new strategy of materials design for light energy harvesting and photodetection.

Keywords: ferroelectrics, BZT-BCT, bandgap, photo-pyroelectric response

1. Introduction

Ferroelectric materials with switchable spontaneous polarization under external electric field show not only remarkable dielectric, piezoelectric, ferroelectric properties, but also intriguing photo-electric conversion capability through bulk photovoltaic effect (BPVE) and pyroelectric effect [1-5]. BPVE stems from the inversion symmetry breaking in ferroelectrics, which enables the separation of photogenerated electron-hole pairs throughout the whole samples, triggering above-bandgap open circuit voltage and fast photoelectric response [6-9]. Pyroelectric effect with the ability of responding to temperature change, can also initiate electrical signals when light conditions change due to the photothermal effect [10-13]. Both effects and their coupling have unfolded giant potential in the field of photodetection and photocatalysis [14-21].

However, the traditional ferroelectric materials including $BaTiO_3$ [22], $BiFeO_3$ [23,24], $KNbO_3$ [6,25,26] and $AgNbO_3$ [7] generally exhibit wide bandgaps (E_g > 2.7 eV) and relative low pyroelectric coefficients ρ, which only allow ultraviolet light absorption and low photo-pyroelectric response. The common improvement strategies are to narrow bandgap and upgrade pyroelectric coefficient ρ by doping [6,10,24,27],

but the simultaneous achievements of both objectives seem challenging. When the B-site element of ABO_3 perovskite-type ferroelectrics is modified or substituted by a hetero-valence transition metal (TM) element to narrow the bandgap, the increase of defects such as oxygen vacancies ($V_O^{\cdot\cdot}$) and electrons partially filled in the d-orbital state ($d^{n\neq0}$) of TM elements enhance leakage current significantly in most cases, which deteriorates severely the ferroelectricity [28,29]. This contradicts with the large polarization and polarization change required by high pyroelectric coefficient [10]. Fortunately, some TM elements exhibiting the eliminated electron degeneracy of d-orbital can cause structural distortion by tilting the $(TM)O_6$ octahedra (i.e., Jahn-Teller (J-T) effect), assisting in the central symmetry breaking, [30-32]. In addition, J-T active ions with $d^{n\neq0}$ can tune bandgap and thus the photoelectric conversion effectively. Thereby, the introduction of J-T active ions into ferroelectrics may have a positive effect on developing high performance ferroelectrics with narrow bandgaps. Mn^{3+} is a typical J-T active ion and reported that it made the phase transition temperature of $BaTiO_3$ down [32], which may boost pyroelectric response [27,33].

Based on the above consideration, we choose $0.5Ba(Zr_{0.2}Ti_{0.8})O_3$-$0.5(Ba_{0.7}Ca_{0.3})TiO_3$ (BZT-BCT) ceramic, a $BaTiO_3$-based ferroelectrics with high piezoelectricity ($d_{33} \approx$ 600 pC/N), high room-temperature pyroelectricity (ρ = 4.80 × 10^{-4} $C{\cdot}m^{-2}{\cdot}K^{-1}$), but wide bandgap of 3.2 eV [34-36] as research object, and investigate the effect of Mn doping on the structure and properties of BZT-BCT by preparing $0.5Ba(Zr_{0.2-x}Ti_{0.8}Mn_x)O_3$-$0.5(Ba_{0.7}Ca_{0.3})TiO_3$ ($BZTM_x$-BCT) ceramics. Compared with the reference samples $0.5Ba(Zr_{0.14}Ti_{0.8}TM_{0.06})O_3$-$0.5(Ba_{0.7}Ca_{0.3})TiO_3$ (TM = non J-T ions Ni^{2+} and Fe^{3+}, denoted as $BZTN_{0.06}$-BCT and $BZTF_{0.06}$-BCT, respectively), both narrow bandgap of 1.2 eV and excellent residual ferroelectric polarization of 9.9 μC/cm^2 are achieved simultaneously in our $BZTM_{0.12}$-BCT ceramic, which greatly expands the photo response to visible and near-infrared light zones. Specifically, benefiting from the increased pyroelectric coefficient and stronger photothermal conversion capability, the photo induced pyroelectric response is increased by over one order of magnitude.

2. Experimental section

2.1. Materials Preparation:

The $0.5Ba(Zr_{0.2-x}Ti_{0.8}Mn_x)O_3$-$0.5(Ba_{0.7}Ca_{0.3})TiO_3$ (abbreviated as $BZTM_x$-BCT) (where x = 0, 0.02, 0.04, 0.06, 0.08, 0.10, 0.12), and $0.5Ba(Zr_{0.14}Ti_{0.8}TM_{0.06})O_3$-$0.5(Ba_{0.7}Ca_{0.3})TiO_3$ (TM = Ni^{2+}, Fe^{3+}, abbreviated as $BZTN_{0.06}$-BCT and $BZTF_{0.06}$-BCT, respectively) ferroelectric ceramics were prepared by a conventional solid phase sintering method. The raw materials $BaCO_3$ (99.0%), $CaCO_3$ (99.0%), $BaZrO_3$ (99.0%), TiO_2 (98.0%), MnO_2 (99%), NiO (99%), and Fe_2O_3 (99%) were weighted according to the stoichiometric ratio and then mixed in ethanol, following which the mixture was handled in the sequence of ball milling in a PTFE jar for 10 hours, drying at 80 ℃ in a drying oven and pre-calcining at 1300 ℃ for 4 hours. The products were ground by hand for 30 min, followed by repeated steps as above. After third ball milling, the sample powders were mixed with a certain amount of binder (5 wt% of polyvinyl alcohol dissolved in deionized water) and uniaxially pressed into discs with a diameter of 10 mm under 30 MPa. The discs were sintered at 1450 ℃ for 6 hours to obtain the final ceramic samples.

2.2. Characterization

The X-Ray diffractometer with Cu K_α radiation (XRD, Bruker D8 ADVANCE, Germany) was used to examine the crystalline phase and lattice structure. The microstructure and elements distribution of ceramics were characterized by field emission scanning electron microscopy (FESEM, ZEISS GeminiSEM 300, Germany) and transmission electron microscopy (TEM, JEM-2100F, JEOL, Japan). Raman spectroscopy is collected with a Raman scattering spectrophotometer (HR EVOLUTION, HORIBA, France). The light absorption measurement was conducted on a PerkinElmer Lambda 900 UV-Vis-NIR spectrometer with an integrating sphere covered with $BaSO_4$ as reference. The X-ray photoelectron spectroscopy (XPS, Thermo Scientific K-Alpha) was used to identify the valence state of element and the energy band structures. Silver electrodes were covered on both sides of ceramics for

electric measurements. The ferroelectric testing system (TF2000E analyzer, axiACCT, Germany) was used to test the polarization-electric field (P-E) curves. The piezoelectric coefficient d_{33} of samples poled at 35 kV/cm was measured by a quasi-static d_{33} meter (ZJ-6A, Institute of acoustics, China). The dielectric property was collected with the dielectric temperature spectrum measuring system (DM-2000, Partulab). Samples with sizes of 7 × 5 × 0.5 mm were used for photoelectric measurement. For photovoltaic test, Au plane electrodes structure with a gap of 0.5 mm on the ceramic surface was configured. Before tests, the bulk samples were poled under 30 kV/cm dc electric field. For photo-pyroelectric measurement, the ceramics covered with Ag electrodes on both sides were polarized by AC electric field of 40 kV/cm firstly. Then the Ag electrode on one side was removed and ITO electrode was deposited as an alternative. The current signals were recorded via a high precision electrometer (Keithley 6517B) and the light used were Xenon lamp light (300~2500 nm) and near-infrared light (800~2500 nm). A thermocouple was used to record the temperature variation during the measurements.

3. Results and discussion

3.1. Structural characterization

Fig. 1a shows the X-ray diffraction (XRD) patterns of TM-doped BZT-BCT (TM = Mn, Ni and Fe) ceramics at room temperature (RT, about 28°C). All the patterns are indexed to perovskite phase close to tetragonal $BaTiO_3$ (PDF#79-2265) and no impurity phases are detected. The (200) and (220) peaks are extracted and magnified in Fig. 1b. As previously reported, the parent BZT-BCT ceramic indicates the coexistence of tetragonal (T), orthorhombic (O) and rhombohedral (R) phase, proved by the merging of (200)/(002) peaks and (202)/(220) peaks in composition x = 0 [34,37,38]. However, with increasing the doping content of Mn, the (200)/(002) peaks and (202)/(220) peaks shift to higher angles and present obvious asymmetric splitting, manifesting the phase transition from the multi-phase coexistence state to T phase. By contrast, $BZTN_{0.06}$-BCT and $BZTF_{0.06}$-BCT ceramics only show single (200) and (220) peaks, typifying the occurrence of considerable cubic phase in the Ni^{2+} and Fe^{3+}

doping BZT-BCT ceramics at lower doping concentration. Identical results are further confirmed by the temperature dependent relative permittivity, from which the decreasing tetragonal-cubic phase transition temperatures are also observed (Fig. S1). The transgranular fracture of cross-section and uniform element distributions of $BZTM_{0.12}$-BCT ceramics characterized by SEM and EDS demonstrate excellent quality of ceramics (Fig. S2).

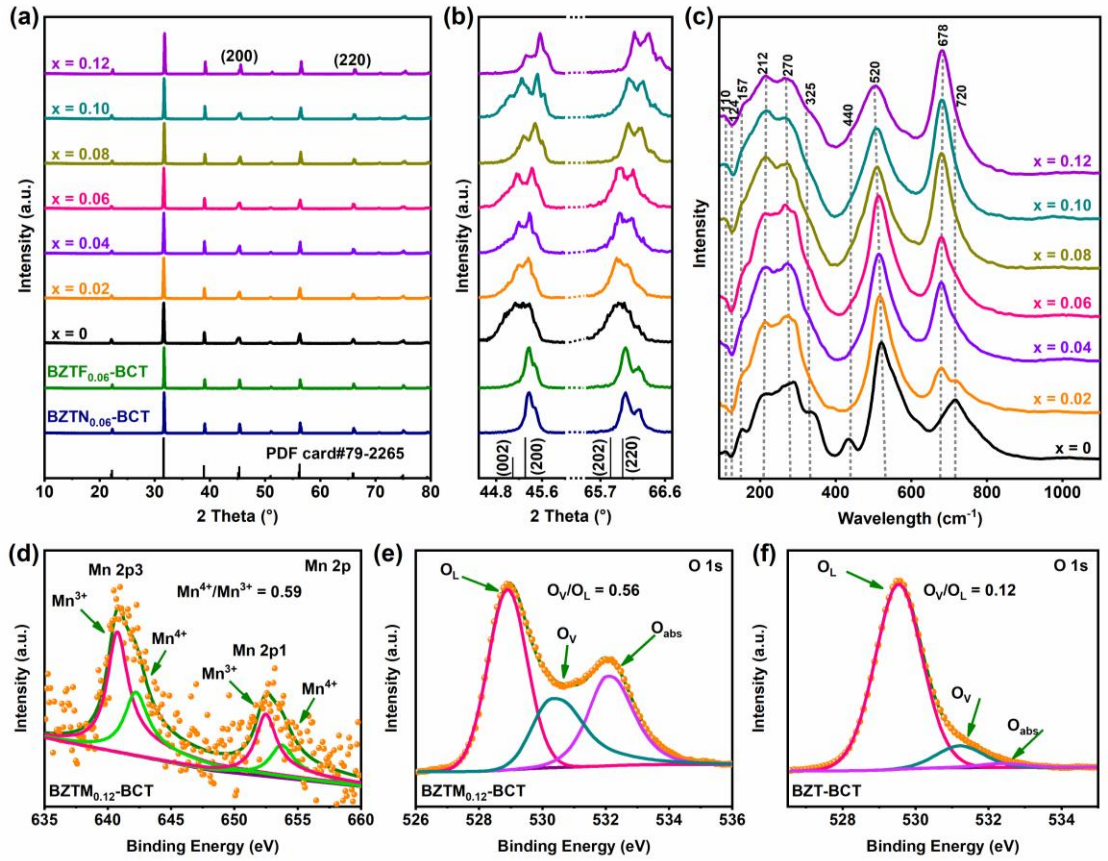

Fig. 1. XRD, Raman and XPS analysis results. (a) The XRD patterns of $BZTM_x$-BCT (x = 0~0.12), $BZTN_{0.06}$-BCT and $BZTF_{0.06}$-BCT ceramics. (b) The magnified parts of (200) and (220) peaks in (a). (c) Raman spectra of $BZTM_x$-BCT ceramics collected at room temperature. (d-f) XPS spectra of Mn2p in $BZTM_{0.12}$-BCT (d), O1s in $BZTM_{0.12}$-BCT (e) and O1s in pristine BZT-BCT (f).

The Raman spectra of $BZTM_x$-BCT are collected to further analyze the local structure details (Fig. 1c). Taking $BaTiO_3$ as a reference [39], the "triple mode" in the parent BZT-BCT ceramic consisting of peaks at 110, 157 and 212 cm^{-1} is regarded as an indicator of the R phase, among them, the peak at 110 cm^{-1} is attributed to the Zr-O

motion [40]. The mode at 270 cm^{-1} ascribed to the A1(TO), together with the mode at 440 cm^{-1} confirm the existence of O phase [41].The modes at 325, 520 and 720 cm^{-1}, assigned to the B1(TO)/E(TO+LO), E(TO)/A1(TO) and A1(LO)/E(LO), respectively, are the symbols of T phase, [28,42], in which the former is related to the displacement of Ti^{4+}/Zr^{4+}, and the latter two stem from oxygen vibrations in Ti/ZrO_6 octahedra. Besides, the dip at 124 cm^{-1} caused by the interference effect between A1(TO) phonons is attributed to the different ionic radius of Zr^{4+} and Ti^{4+} and also shows the B-site ion order [40,43]. All the results confirm the presence of long-range ferroelectric polar order and indicate the coexistence of R, O and T phase in BZT-BCT. In $BZTM_x$-BCT ($x > 0$) ceramics, due to the increasing Jahn-Teller distortion with increasing x, the mode at 720 cm^{-1} shifts to near 678 cm^{-1} [44], and the mode at 520 cm^{-1} broadens and moves down to 504 cm^{-1} because of heavier atomic mass of Mn than Zr element (Fig. S3) [45]. The absence of mode at 440 cm^{-1} manifests the disappearance of O phase. The retained "triple mode" at low frequency, A1(TO), E(TO)/A1(TO) and A1(LO)/E(LO) modes confirm that the R and T phase still coexist after Mn doping.

The Mn2p XPS spectrum with asymmetric feature shows multivalence states of Mn element in $BZTM_{0.12}$-BCT composition (Fig. 1d and S4). Mn^{3+} and Mn^{4+} are recognized by the peaks at 640.74 eV and 652.48 eV and the peaks at 642.22 eV and 653.74 eV, respectively [46]. The amount ratio of Mn^{3+}/Mn^{4+} is estimated to be 1.7, indicating that the Mn^{3+} is dominant in the $BZTM_{0.12}$-BCT ceramic, which explains the lattice shrinkage presented in XRD. In order to maintain electric neutrality, a far higher concentration of oxygen vacancies (O_V) (56%) than that in virgin BZT-BCT (12%) appears in $BZTM_{0.12}$-BCT ceramic (Fig. 1e,f). The peaks at 529.54 eV, 531.22 eV and 532.38 eV are ascribed to lattice oxygen (O_L), oxygen vacancies (O_V) and adsorption oxygen (O_{abs}), respectively [47].

TEM analysis was used to understand the microstructure of $BZTM_{0.12}$-BCT ceramic. As shown in Fig. 2a, a large number of irregular stress fringes were detected while only a few regulated ferroelectric domain-walls were observed in the grains. Meanwhile, the diffraction spots in the selected area electron diffraction (SAED)

pattern of Grain-1 along [100] direction show a remarkable splitting phenomenon (Fig. 2b), suggesting the local multi-orientation/multi-phase coexistence state of the grains. This phenomenon agrees well with the results of Raman analysis and is a typical characterization of ferroelectrics located at the morphotropic phase boundary (MPB) regions. The dark field image of the Grian-1 further confirms the local multi-orientation/multi-phase coexistence states of the ceramic. As shown in Fig. 2c, the grains were divided into a large number of nano-domain areas. To make clear the structural nature of the nano-domains, the local lattice strain/stress fields were calculated by the geometric phase analysis (GPA) method on an HRTEM image of Grain-1. As shown in Fig. 2d-g, the strain states certainly change with the position and the lattices could be divided into several strain zones, corresponding to the nano-domains. The region divisions are different among the in-plane strain tensor components ε_{xx}, ε_{yy}, shear ε_{xy}, and lattice rotation ω_{xy}, suggesting the complicated orientations/phase-structure relationships among the nano-domains. Additionally, what is worth noting is that the strain states significantly fluctuate in the domain regions. To directly observe and understand the strain fluctuation, the HRTEM of the local lattice was taken and given in Fig. 2h. It can be seen that a point-defect-like contrast (marked with arrows) could be observed in the lattice though it is difficult to identify by naked eyes. Fig. 2i gives the corresponding pseudo-color image of the fast Fourier transformation (FFT)-filtered HRTEM image by using (010), $(01\bar{0})$, (001), and $(00\bar{1})$ points as calculating spots. The point-defects are figured prominently in the image. Considering the effect of the high density of point-defects on the properties of $BZTM_{0.12}$-BCT ceramic, it can be speculated that it could lead to the unstable state of local polarization and, on the other hand, it could significantly increase the photo absorption effect of the sample. The interactions of them will inevitably improve the photo-electric coupling function of the $BZTM_{0.12}$-BCT ceramic and contribute to the strong photo-pyroelectric effect.

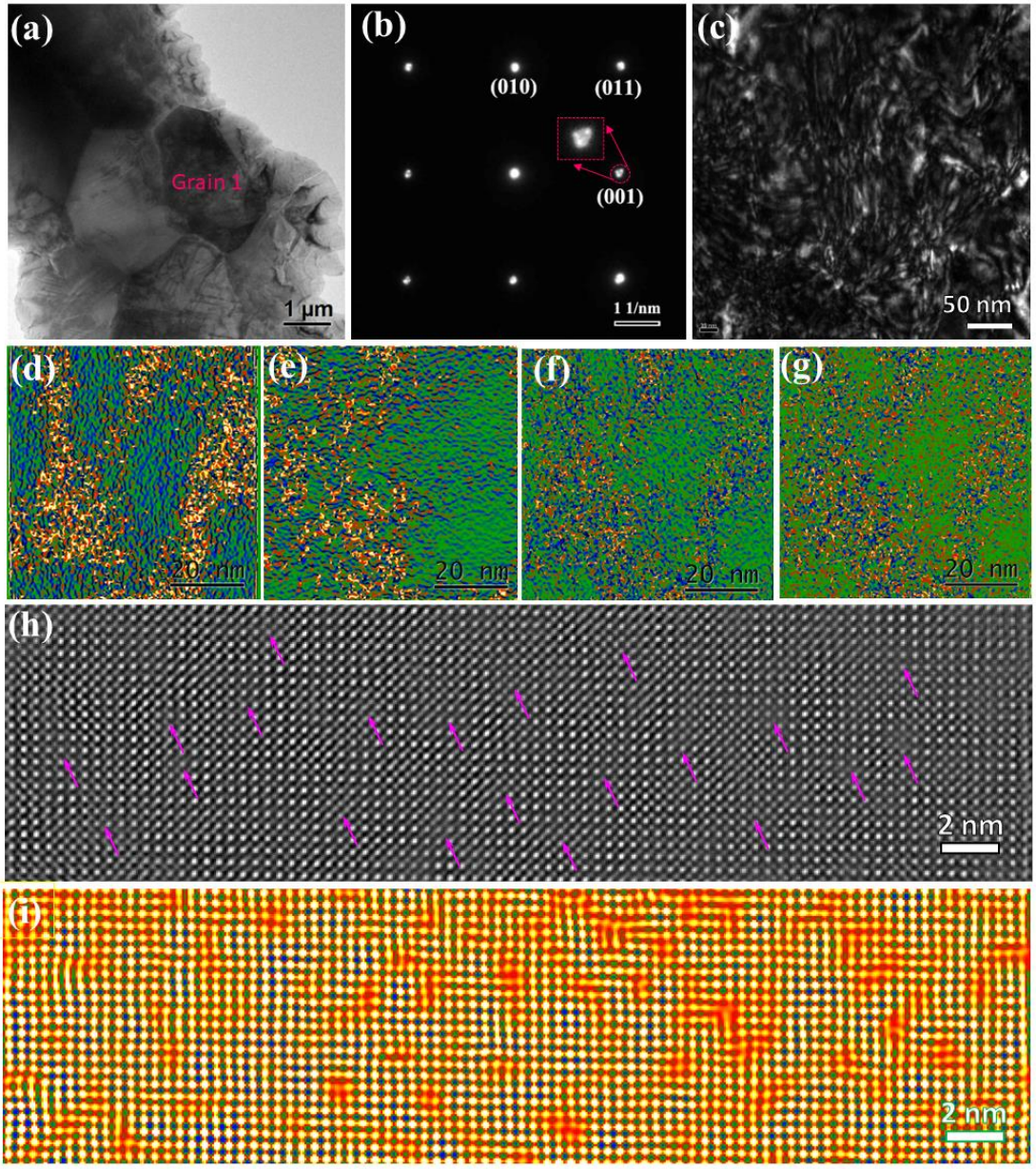

Fig. 2. TEM analysis of $BZTM_{0.12}$-BCT ceramic. (a) Morphological image of the grains. (b) SAED pattern of Grain-1 taken along [100] zone axes. (c) Dark-field image of [100]-oriented Grain-1 by using (001) point as imaging spot. (d-g) Local in-plane strain tensor components ε_{xx}, ε_{yy}, shear ε_{xy}, and lattice rotation ω_{xy} deduced by GPA. (h) HRTEM image of the local lattice of [100]-oriented Grain-1, and (i) Corresponding pseudo-color image of the fast Fourier transformation (FFT)-filtered HRTEM image by using (010), $(01\bar{0})$, (001), and $(00\bar{1})$ points as calculating spots.

3.2. Bandgaps evolution

Fig. 3a shows UV-vis-NIR light absorption spectra of the BZTM$_x$-BCT ceramic powders. With increasing the content of Mn, light absorption wavelengths of the samples extended from below 400 nm of pristine BZT-BCT to near infrared light (over 1500 nm) of BZTM$_x$-BCT, accompanying with sample colors change from white to dark brown. This ultrabroad photoabsorption capability is rarely observed in other ferroelectric materials. The bandgaps are calculated according to the Tauc's rule, $(\alpha h\nu)^2 = A(h\nu - E_g)$, where α, $h\nu$ and A are the absorption coefficient, photon energy and constant, respectively (Fig. 3b,c). Unlike the pure BZT-BCT sample (E_g = 3.2 eV), two different gap states appear in BZTM$_x$-BCT samples and these gap states present a redshift with increasing x, similar to the reported Mn and Co-mediated $BaTiO_3$ [42,45]. The lowest bandgap E_{g1} of 1.9 eV and sub-bandgap E_{g2} of 1.2 eV are obtained in BZTM$_{0.12}$-BCT, which is beneficial to the generation of above-bandgap photoexcited electrons and holes. These electrons and holes then relax to the conductive band minimum (CBM) and valance band maximum (VBM), releasing more heat than wide bandgap BZT-BCT sample (Fig. 3d), as discussed later. The position variations of VBM and CBM with x in BZTM$_x$-BCT are determined by the VB-XPS measurement (Fig. S5). The VBM moves up gradually and CBM moves down significantly at low Mn doping content, and then they change slowly at high doping content, which reduces dramatically the bandgap of BZT-BCT samples.

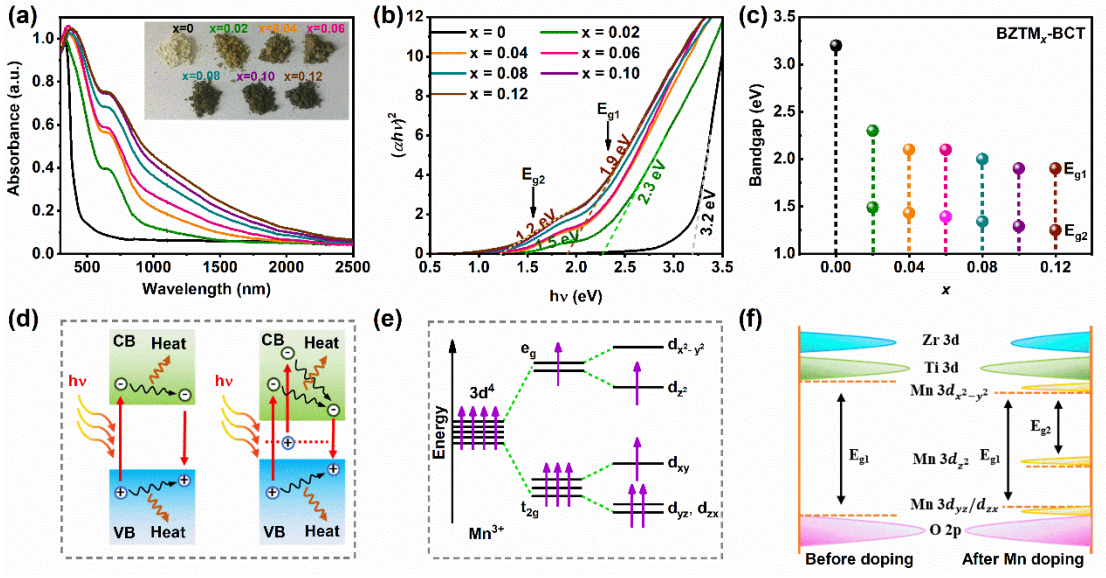

Fig. 3. Photo absorption and band structure analyses of BZTM$_x$-BCT ceramics. (a)

UV-vis-NIR absorption spectra. Inset is photos of the samples. (b) The fitting plot of bandgaps according to the Tauc's rule. (c) The variations of bandgaps with *x*. (d) Schematic of electron generation, relaxation and recombination in wide and narrow bandgap ferroelectric semiconductors. (e) Electron configuration in 3d orbital of Mn^{3+}. (f) Energy band structures of BZT-BCT ceramics (left) before and (right) after Mn doping.

To further understand the abnormal multi-bandgap states in BZTM$_x$-BCT, Fig. 3e,f schematically illustrate the possible electron transition processes. In BZT-BCT sample, the Ti3d and O2p orbitals constitute the CBM and VBM, respectively [48], resulting in the bandgap of 3.2 eV. As for the BZTM$_x$-BCT compositions, due to the eliminated electron degeneracy, the Mn^{3+} $3d^4$ orbital is split into two high energy e_g states (half-filled d_{z^2} and unfilled $d_{z^2-y^2}$) and three low energy t_{2g} states (half-filled d_{xy}, d_{yz}, d_{zx}) under anisotropic crystal field of ferroelectrics, in which $d_{z^2-y^2}$ locates near CBM and $d_{yz}/d_{zx}/d_{xy}$ locate near VBM (Fig. 3e) [24,49]. In high spin complex formed by Mn^{3+}, the high electron pairing energy impels the electrons preferentially to occupy the unfilled rather than the half-filled state firstly to keep the lowest energy of the system. Therefore, the E_{g1} and E_{g2} can be attributed to the electron hoping from the orbitals of $d_{yz}/d_{zx}/d_{xy}$ and d_{z^2} to $d_{z^2-y^2}$, respectively (Fig. 3f). The gap state caused by d_{z^2} is also observed in TM-doping $BiFeO_3$ and Ni^{2+}-mediated $Na_{0.5}Bi_{0.5}TiO_3$ [8,24].

3.3. Polar properties

Fig. 4a shows P-E loops of the BZTM$_x$-BCT ceramics. Though they exhibit low bandgaps from 1.5 to 1.2 eV and high concentration of oxygen vacancies, the textbook-like saturated polarization-electric field (*P*-*E*) hysteresis loops confirm well-maintained ferroelectricity after Mn doping. For clarity, the ferroelectricity between BZTM$_x$-BCT and parent BZT-BCT ceramics are compared in Fig. 4b. The residual polarization (P_r) values of all the samples maintain over 60% of pure

BZT-BCT (P_r = 12.7 μC/cm^2). The composition x = 0.08 and 0.12 exhibit slightly more superior maintenance of 76.5%, corresponding to the P_r of 9.9 μC/cm^2. The saturated polarizations of BZTM$_x$-BCT ceramics at maximum electric field (P_{sat}) unfold over 88% P_{sat} (about 15.6 μC/cm^2) of pristine BZT-BCT (P_{sat} = 17.7 μC/cm^2). Concurrently, all the BZTM$_x$-BCT ceramics shows large piezoelectric coefficient over 100 pC/N (Fig. S6). The combination of excellent ferroelectricity/piezoelectricity and narrow bandgap in BZTM$_x$-BCT surpasses common ferroelectric photovoltaic materials (Fig. 4c and Table S1). In contrast, the ferroelectricity and piezoelectricity of BZTN$_{0.06}$-BCT and BZTF$_{0.06}$-BCT ceramics are weakened severely due to the almost disappeared polarity preferred phase (Fig. 4d and S6). Due to higher concentration of O_V in BZTM$_{0.12}$-BCT than in BZT-BCT ceramic, the domain switching is pinned, resulting in larger coercive field and build-in electric field E_{bi} (E_{bi} = $|E_C^+ + E_C^-|/2$, E_C^+ and E_C^- are positive and negative coercive fields, respectively) after Mn doping. However, no significant increasing leakage is observed in BZTM$_{0.12}$-BCT ceramic (Fig. 4e,f). As a result, the commonly used co-doping strategy is unnecessary in BZTM$_x$-BCT ceramics. On one hand, the Jahn-Teller distortions of Mn^{3+} stabilize the ferroelectricity [32]. On the other hand, Mn doping effectively suppress O_V diffusion and trap the electrons through forming Mn'_{Ti}-$V_O^{\cdot\cdot}$ combination and changing valance states [49-51]. Even under light illumination, the polar behaviour remains well. The slight increase of dielectric constant (ε) and slight decrease of P_r values are due to the photothermal effect (Fig. S7 and S8).

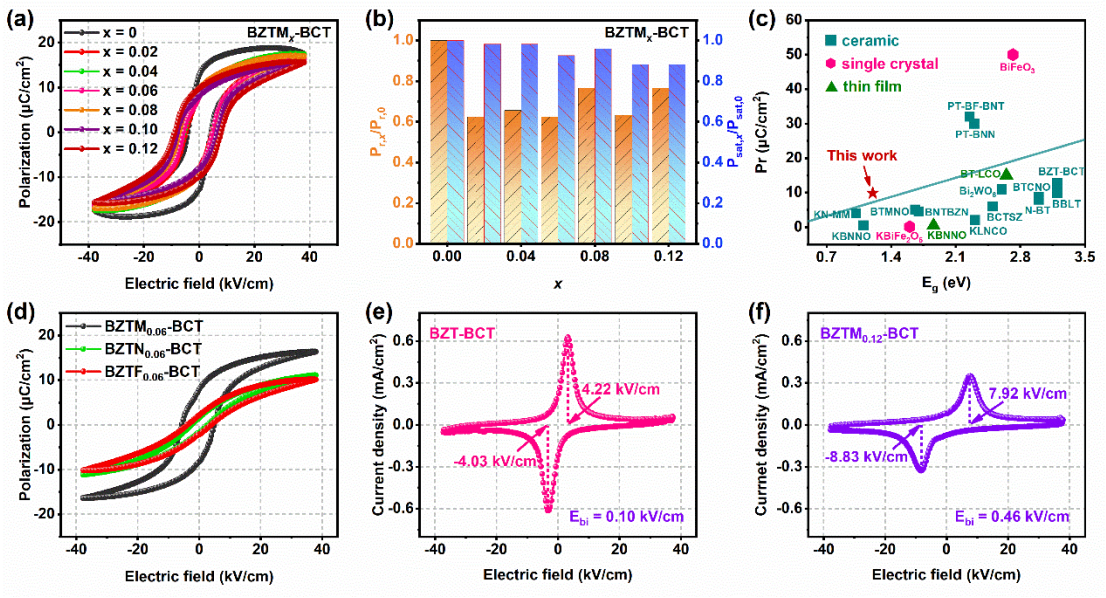

Fig. 4. Polar properties of BZTM$_x$-BCT, BZTN$_{0.06}$-BCT and BZTF$_{0.06}$-BCT ceramics measured at room temperature. (a) Polarization-electric field (*P*-*E*) loops. (b) The variation of the ratios between residual polarization ($P_{r,x}$) and saturated polarization ($P_{sat,x}$) of BZTM$_x$-BCT and BZT-BCT ($P_{r,0}$, $P_{sat,0}$) ceramics with *x*. (c) Summary of the bandgap and residual polarization of known ferroelectric materials. The references are listed in Table S1. (d) The ferroelectricity comparison of BZTM$_{0.06}$-BCT, BZTN$_{0.06}$-BCT and BZTF$_{0.06}$-BCT ceramics. (e,f) The current density-electric field curves of BZT-BCT (e) and BZTM$_{0.12}$-BCT ceramics (f).

3.4. Photoelectric properties

Based on the excellent ferroelectric maintenance and wide-spectral light absorption, the BZTM$_{0.12}$-BCT ceramic is selected for the photoelectric measurement through a plane electrodes configuration with Au electrodes (Fig. 5a). The photoelectric responses under white light (300~2500 nm) and near-infrared (NIR) light (800~2500 nm) of 100 mW/cm^2 are summarized. The Au/BZTM$_{0.12}$-BCT/Au device shows switchable photocurrent under different polarization states and almost linear current-voltage (*I*-*V*) curves (Fig. 5b,c), indicating the Ohmic contact between electrodes and ceramic. Benefiting from the ultrabroad photo absorption capacity, the open circuit voltages (V_{oc}) and short circuit currents (I_{sc}) are 0.5 V/46 pA and 0.4 V/24 pA under white and NIR light, respectively. The I_{sc} ratio between NIR and white

light contributing to photoresponse reach 52%. The zero-bias photocurrent curves (*I-t*) of $BZTM_{0.12}$-BCT and BZT-BCT ceramics under periodic light turning on/off are presented in Fig. 5d,e. The *I-t* curves can be divided into three parts, i.e., the positive and negative peak currents (I_{py}) attributed to pyroelectric effect and platform current (I_{ph}) related to photovoltaic effect. Comparing with pristine BZT-BCT ceramic, the photovoltaic (Fig. 5f) and pyroelectric responses of $BZTM_{0.12}$-BCT ceramic are improved by nearly one order of magnitude, especially in the pyroelectric response. With the low dark current (about 1 pA), large on/off ratio of about 10^3 is obtained. These results indicate great potential for the application in photodetection.

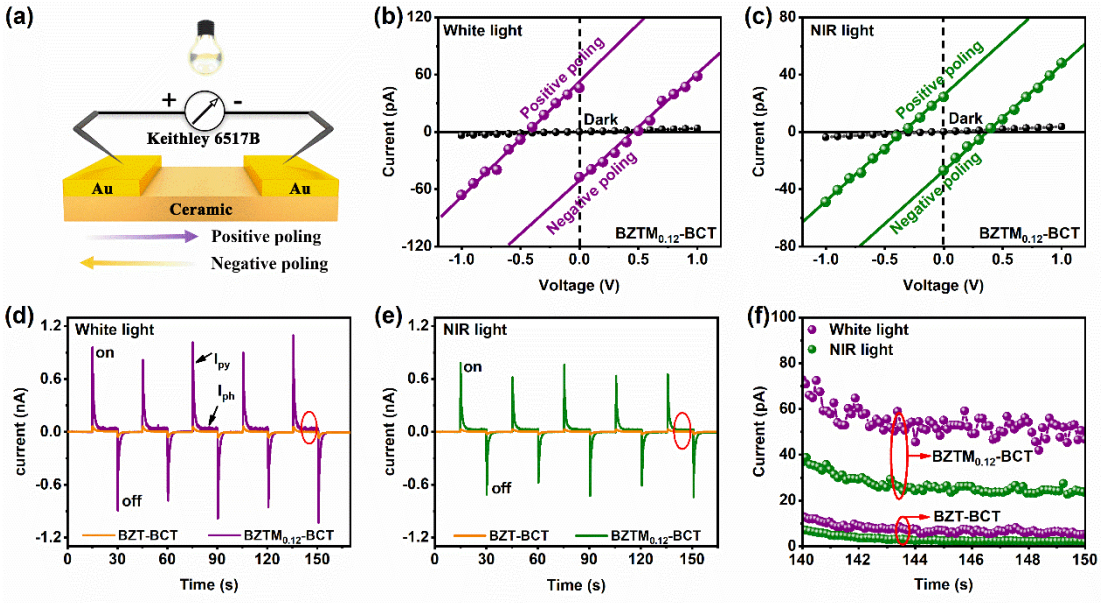

Fig. 5. Photoelectric properties characterization under light intensity of 100 mW/cm^2. (a) The plane electrodes configuration for photoelectric measurement. (b,c) Photocurrent-voltage (*I-V*) curves of $BZTM_{0.12}$-BCT ceramic under white light (300~2500 nm) and NIR light (800~2500 nm), respectively. (d,e) Photocurrent-time (*I-t*) curves of $BZTM_{0.12}$-BCT and BZT-BCT ceramics under periodic white light and NIR light. On and off mean light turning on/off. (f) Replot showing details of the current platform part in (d,e).

The significantly enhanced pyroelectric response deserves in-depth study. In order to calculate the pyroelectric parameters precisely, an up-down electrodes configuration by ITO/$BZTM_{0.12}$-BCT/Ag is used to investigate the NIR light induced

pyroelectric response (Fig. S9). With increasing light intensities from 20 to 100 mW/cm^2, the temperature changes (ΔT) increase from 0.63 to 3.03 ℃, corresponding to the maximum temperature change rates (*dT/dt*) from 0.06±0.02 to 0.46±0.03 ℃/s (Fig. S10). The faster rising temperature rate at higher light intensity makes the maximum pyroelectric current/open circuit voltage (I_{py}/V_{oc}) gradually increase from 2.7 nA/1.1 V to 16.9 nA/5.3 V (Fig. 6a). However, the ΔT of BZT-BCT ceramic is only about 2 ℃ with maximum *dT/dt* of 0.37±0.04 ℃/s under light of 100 mW/cm^2 (Fig. S11). The ΔT and *dT/dt* markedly improve firstly and then change slowly with increasing the Mn doping content, which agrees well with the change trend of bandgap. Obviously, the increase of ΔT and *dT/dt* is very beneficial to the improvement of pyroelectric output. The stronger photothermal conversion after Mn doping stems from the relaxation and recombination of more photoexcited carriers in $BZTM_{0.12}$-BCT ceramic caused by lower bandgap and high density of point defects. For clarity, the variations of maximum *dT/dt*, I_{py} and V_{oc} of $BZTM_{0.12}$-BCT ceramic with light intensities are fitted in Fig. 6b. The ITO/$BZTM_{0.12}$-BCT/Ag device shows almost linear relationship between pyroelectric output and light intensities with current and voltage sensitivities of 0.169 nA/(mW·cm^{-2}) and 0.052 V/(mW·cm^{-2}), respectively, which benefits the precise control of infrared light pyroelectric devices. This response can be further improved by optimizing the electrodes [52]. Pyroelectric coefficient is an important parameter to estimate the pyroelectric properties. According to $\rho = I_{py} \cdot S^{-1} \cdot (dT/dt)^{-1}$, where *S* is the effective electrode area [28], the estimated ρ of $BZTM_{.0.12}$-BCT near RT is (5.83±0.36)×10^{-8} C·cm^{-2}·K^{-1}, higher than (4.50±0.43)×10^{-8} C·cm^{-2}·K^{-1} of pure BZT-BCT ceramic and the reported values of common lead-free pyroelectric materials like KNN and BNT ceramics, etc. (Table S2) [53,54]. The MPB region and the decreasing phase transition temperature play important role in the high ρ of $BZTM_{0.12}$-BCT ceramic. Consequently, the simultaneous improvements in *dT/dt* and ρ contribute to the enhancement of photo-pyroelectric output. The response time and recovery time, defined as the time for the current increasing from 10% to 90% of positive current peak and the current decreasing from 90% to 10% of negative current peak, are estimated to be <0.03 s and

15.42 s, respectively (Fig. S12). Under real sunlight irradiation accompanied with the light intensity of 84.2 mW/cm^2 and ambient temperature of 41 ℃, the maximum I_{py} of ITO/BZTM$_{0.12}$-BCT/Ag device are 13.2/-14.6 nA, verifying the signal acquisition capability in real conditions (Fig. 6c). The stability of the ITO/BZTM$_{0.12}$-BCT/Ag device is also confirmed by the periodic illumination over 100 cycles (Fig. 6d). These results confirm the potential of BZTM$_{0.12}$-BCT in near-infrared photoelectric devices and multi-source energies conversion.

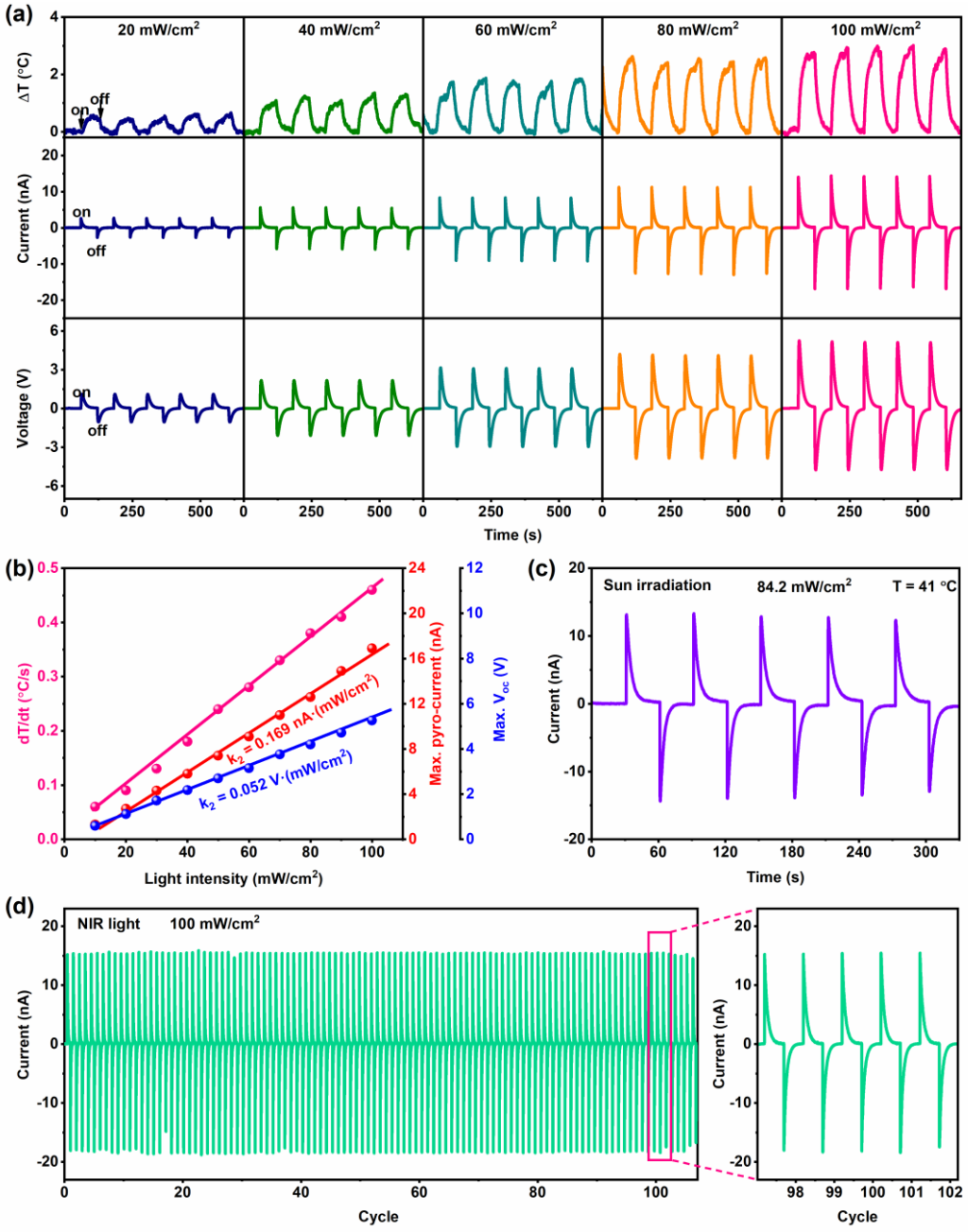

Fig. 6. Photo-pyroelectric properties of BZTM$_{0.12}$-BCT ceramic. (a) Time and NIR

light intensities dependence of temperature change (ΔT), photocurrent (I_{py}) and photovoltage (V_{oc}) at zero bias. (b) The maximum dT/dt, I_{py} and V_{oc} versus NIR light intensities. (c) Pyroelectric response under real sun irradiation with light intensity of 84.2 mW/cm^2 and ambient temperature of 41 ℃. (d) The stability measurement for $BZTM_{0.12}$-BCT's pyroelectric property.

As a show case, we further used the device to detect human body. The wavelength of human body infrared irradiation is in the range of 3~50 μm, and about half of the irradiation energy is concentrated in 8~14 μm, which is difficult to be detected by conventional semiconductor-based photodetectors. Instead, the pyroelectric detectors indicate the superiority of ultrabroadband spectral detection. Fig. 7a and Video S1 schematically show the infrared detection of human hand by the ITO/$BZTM_{0.12}$-BCT/Ag device. When the hand is placed about 1 cm above the device, the power intensity irradiated on the device is about 2.57 mW/cm^2, and the pyroelectric output of about 0.9 nA and 0.4 V are observed (Fig. 7b,c). Even the distance between human hand and device increases to 10 cm, The extremely reduced infrared radiation intensity can still be clearly detected (Fig. S13). Differently, the pyroelectric currents of some other irradiation sources, including metal, glass, plastic and paper, are almost invisible (Fig. S14), which confirms the strong anti-interference ability of our human body infrared detector to the environmental factors. The ITO/$BZTM_{0.12}$-BCT/Ag devices with ceramic sizes of 6×3×0.5 mm^3 are glued on a Copper foil and designed as a 5×7 array to indicate the potential application of $BZTM_{0.12}$-BCT ceramic (Fig. 7d). As shown in Fig. 7e,f, for "palm" and "fist" gestures, different patterns are pictured, indicating the ability to human body imaging. Intuitively, the pyroelectric currents of pixels in hand-covered regions are significantly higher than that in the uncovered regions. It's straightforward that more details of hand will be taken when we further enhance the number of pixels and optimize the structure design of device arrays.

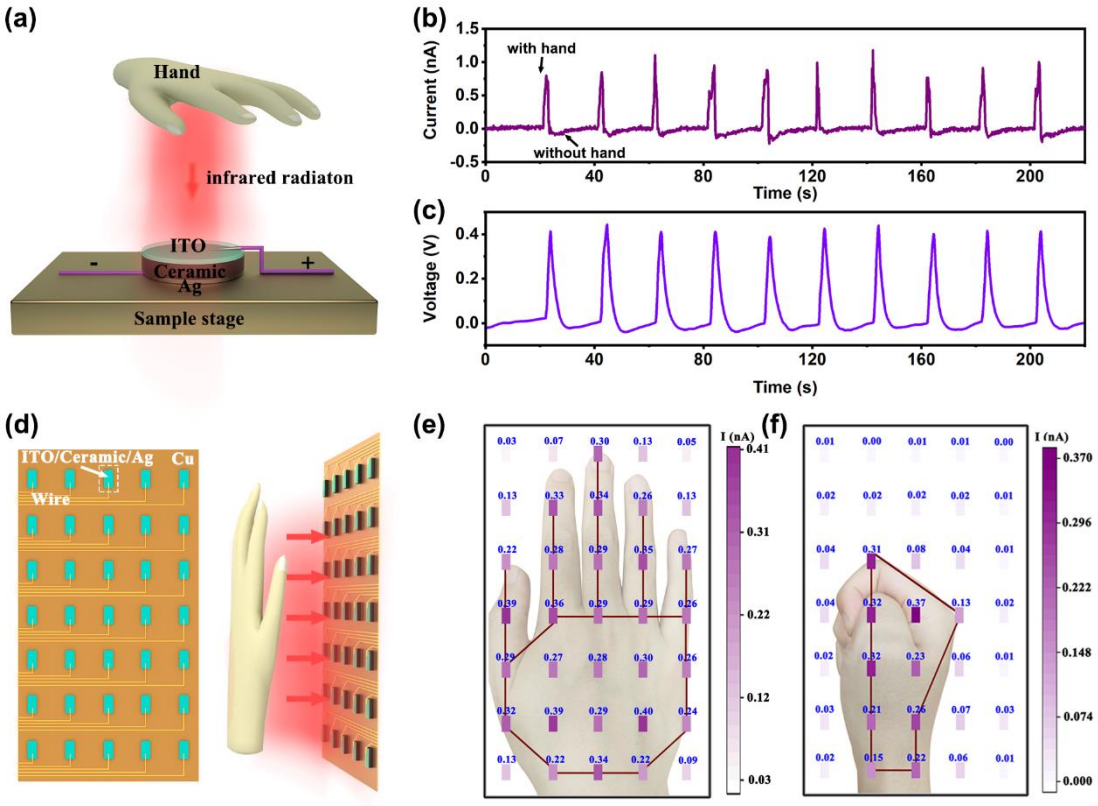

Fig. 7. Device design for human body infrared photodetection demonstration. (a) Schematic diagram of human body infrared detection. (b,c) Pyroelectric current and voltage of $BZTM_{0.12}$-BCT ceramic for human body infrared irradiation. (d) The schematic diagram of a 5×7 array prepared by ITO/$BZTM_{0.12}$-BCT/Ag devices. (e,f) The response signals comparison of "palm" and "fist".

3.5. Discussion

The difference between photo induced photovoltaic and pyroelectric response is schematically explained in Fig. 8. For photovoltaic response in this work, the Schottky barrier caused by the asymmetric electrodes is excluded because both electrodes are formed by Au. Instead, the build-in electric field in the bulk stemming from ferroelectric polarization and the decreasing electrons (holes) transport barrier height at polarization vector head (tail), promotes the separation and flowing of photogenerated carriers (Fig. 8a). Pyroelectric response is associated to polarization fluctuation when the ceramic surface temperature changes (Fig. 8b). With the application of light, the instantly increased temperature ($dT/dt > 0$) engenders the

larger oscillation of electric dipoles around their orientation axes, leading to that the free carriers release from the surface of ceramic and flow through external circuit to generate a positive peak current. Under continuous illumination, the temperature gradually becomes stable (dT/dt = 0), therefore, the I_{py} disappears after a period of time. When the light is turned off, due to the opposite temperature and polarization variations on ceramic surface, a negative peak current generates and ultimately becomes zero. Although BZTM$_x$-BCT samples exist narrower bandgap than BZT-BCT, the increased photogenerated carriers are only partially transported to generate photovoltaic response, while most of them are recombined and relax to the CBM and VBM, resulting in the release of more heat, i.e., larger dT/dt (Fig. 3d). Consequently, the more intense polarization fluctuation causes better pyroelectric response in BZTM$_x$-BCT than BZT-BCT samples. The weak photovoltaic but strong pyroelectric response in this work confirms the assumption that the introduction of J-T active Mn^{3+} ions may have a positive effect on developing high performance ferroelectrics with narrow bandgaps.

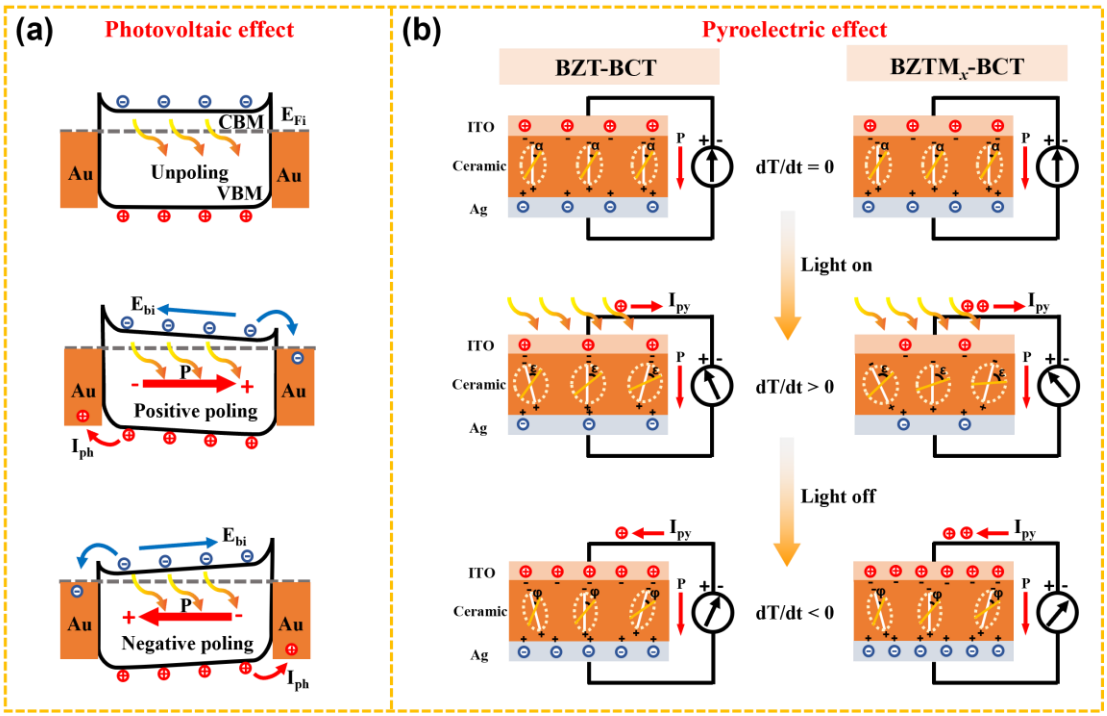

Fig. 8. The difference between light induced photovoltaic and pyroelectric response. (a) The energy band structures of BZTM$_x$-BCT ceramics under different poling conditions. (b) The schematic diagram of polarity changes in BZT-BCT and

$BZTM_x$-BCT based photoelectric devices under different light conditions.

4. Conclusions

In summary, Mn^{3+}-mediated BZT-BCT ceramics with narrow bandgap and excellent ferroelectricity are obtained. More significantly, due to the increase of pyroelectric coefficient and stronger photothermal conversion capability in $BZTM_x$-BCT ceramics, the photo induced pyroelectric current under NIR light improves by one order of magnitude. The pyroelectric device fabricated from the $BZTM_{0.12}$-BCT ceramic demonstrates high sensitivity to the human hand infrared irradiation, exhibiting the potential application for human body monitoring. Our results present an effective strategy to design ferroelectric photoelectric material by utilizing Jahn-Teller (J-T) effect of selected transition metal ion for infrared detection and energy harvesting device applications.

CRediT authorship contribution statement

Lu Wang: Conceptualization, Data curation, Formal analysis, Investigation, Methodology, Software, Validation, Visualization, Writing - original draft, Writing - review & editing. **Faqiang Zhang:** Date curation, Formal analysis, Funding acquisiton, Investigation, Methodology, Software, Writing - original draft, Writing - review & editing**. Chen Chen:** Conceptualization, Formal analysis, Funding acquisition, Methodology, Supervision. **Xiang He:** Formal analysis, Funding acquisition, Validation. **Muzaffar Ahmad Boda:** Visualization, Software. **Kui Yao:** Conceptualization, Methodology, Project administration, Writing - review & editing**. Zhiguo Yi:** Conceptualization, Formal analysis, Funding acquisition, Investigation, Supervision, Valigation, Writing - review & editing, Project administration.

Declaration of Competing Interest

The authors declare that they have no known competing financial interests or personal relationships that could have appeared to influence the work reported in this paper.

Data availability

Date will be made available on request.

Acknowledgements

This work was supported by the National Natural Science Foundation of China (Grant Nos. 51872311 and 52202152), the Frontier Science Key Project of the Chinese Academy of Sciences (QYZDB-SSW-JSC027), Natural Science Foundation of Shanghai (22ZR1471200), the Shanghai Science and Technology Innovation Action Plan (No. 20ZR1465500), the Instrument Developing Project of Chinses Academy of Sciences (Grant No. ZDKYYQ20180004) and Shanghai Sailing Program (22YF1455600). K Yao acknowledges partial support by A*STAR, Singapore, RIE2020 Advanced Manufacturing and Engineering (AME) Programmatic Fund (Grant No. A20G9b0135).

Appendix A. Supporting information

Supplementary data to this article can be found online

References

[1] Y. Yuan, Z. Xiao, B. Yang, J. Huang, Arising applications of ferroelectric materials in photovoltaic devices, J. Mater. Chem. A 2 (2014) 6027-6041.

[2] C. Paillard, X. Bai, I. C. Infante, M. Guennou, G. Geneste, M. Alexe, J. Kreisel, B. Dkhil, Photovoltaics with Ferroelectrics: Current Status and Beyond, Adv. Mater. 28 (2016) 5153-5168.

[3] A. D. Dupuy, Y. Kodera, J. E. Garay, Unprecedented Electro-Optic Performance in Lead-Free Transparent Ceramics, Adv. Mater. 28 (2016) 7970-7977.

[4] K. Yao, S. Chen, S. C. Lai, Y. M. Yousry, Enabling Distributed Intelligence with Ferroelectric Multifunctionalities, Adv. Sci. 9 (2022) e2103842.

[5] B. Dai, Y. Zhou, X. Xiao, Y. Chen, J. Guo, C. Gao, Y. Xie, J. Chen, Fluid Field Modulation in Mass Transfer for Efficient Photocatalysis, Adv. Sci. 9 (2022) e2203057.

[6] I. Grinberg, D. V. West, M. Torres, G. Gou, D. M. Stein, L. Wu, G. Chen, E. M. Gallo, A. R. Akbashev, P. K. Davies, J. E. Spanier, A. M. Rappe, Perovskite oxides for visible-light-absorbing ferroelectric and photovoltaic materials, Nature 503 (2013) 509-512.

[7] X. He, C. Chen, C. Li, H. Zeng, Z. Yi, Ferroelectric, Photoelectric, and

Photovoltaic Performance of Silver Niobate Ceramics, Adv. Funct. Mater. 29 (2019) 1900918.
[8] H. Xiao, W. Dong, Y. Guo, Y. Wang, H. Zhong, Q. Li, M. M. Yang, Design for Highly Piezoelectric and Visible/Near-Infrared Photoresponsive Perovskite Oxides, Adv. Mater. 31 (2019) e1805802.
[9] S. C. Lai, K. Yao, Y. F. Chen, A battery-less photo-detector enabled with simultaneous ferroelectric sensing and energy harnessing mechanism, Appl. Phys. Lett. 103 (2013) 092903.
[10] Z. Liu, T. Lu, S. Yan, Q. Liao, X. Dong, G. Wang, Y. Liu, Large electrocaloric and pyroelectric energy harvesting effect over a broad temperature range via modulating the relaxor behavior in non-relaxor ferroelectrics, J. Mater. Chem. A 9 (2021) 22015-22024.
[11] N. Ma, K. Zhang, Y. Yang, Photovoltaic-Pyroelectric Coupled Effect Induced Electricity for Self-Powered Photodetector System, Adv. Mater. 29 (2017) 1703694.
[12] M. Kumar, H. Seo, High-Performing Self-Powered Photosensing and Reconfigurable Pyro-photoelectric Memory with Ferroelectric Hafnium Oxide, Adv. Mater. 34 (2022) e2106881.
[13] B. Dai, J. Fang, Y. Yu, M. Sun, H. Huang, C. Lu, J. Kou, Y. Zhao, Z. Xu, Construction of Infrared-Light-Responsive Photoinduced Carriers Driver for Enhanced Photocatalytic Hydrogen Evolution, Adv. Mater. 32 (2020) e1906361.
[14] N. Ma, Y. Yang, Enhanced self-powered UV photoresponse of ferroelectric $BaTiO_3$ materials by pyroelectric effect, Nano Energy 40 (2017) 352-359.
[15] S. Singh, N. Khare, Coupling of piezoelectric, semiconducting and photoexcitation properties in $NaNbO_3$ nanostructures for controlling electrical transport: Realizing an efficient piezo-photoanode and piezo-photocatalyst, Nano Energy 38 (2017) 335-341.
[16] S. Zhang, B. Zhang, D. Chen, Z. Guo, M. Ruan, Z. Liu, Promising pyro-photo-electric catalysis in $NaNbO_3$ via integrating solar and cold-hot alternation energy in pyroelectric-assisted photoelectrochemical system, Nano Energy 79 (2021) 105485.
[17] B. K. Gan, K. Yao, S. C. Lai, Y. F. Chen, P. C. Goh, An Ultraviolet (UV) Detector Using a Ferroelectric Thin Film with In-Plane Polarization. IEEE Electron Device Lett. 29 (2008) 1215-1217.
[18] W. Ji, K. Yao, Y.-F. Lim, Y. C. Liang, A. Suwardi, Epitaxial ferroelectric $BiFeO_3$ thin films for unassisted photocatalytic water splitting, Appl. Phys. Lett. 103 (2013) 062901.
[19] B. Dai, J. Guo, C. Gao, H. Yin, Y. Xie, Z. Lin, Recent Advances in Efficient Photocatalysis via Modulation of Electric and Magnetic Fields and Reactive Phase Control, Adv. Mater. 35 (2023) e2210914.
[20] B. Dai, G. M. Biesold, M. Zhang, H. Zou, Y. Ding, Z. L. Wang, Z. Lin, Piezo-phototronic effect on photocatalysis, solar cells, photodetectors and light-emitting diodes, Chem. Soc. Rev. 50 (2021) 13646-13691.
[21] B. Dai, H. Feng, Z. Li, Y. Xie, Field enhanced photocatalytic disinfection, Sci.

Bull. 67 (2022) 779-783.
[22] S. Pal, A. B. Swain, P. P. Biswas, D. Murali, A. Pal, B. R. K. Nanda, P. Murugavel, Giant photovoltaic response in band engineered ferroelectric perovskite, Sci. Rep. 5 (2018) 8005.
[23] S. Y. Yang, J. Seidel, S. J. Byrnes, P. Shafer, C. H. Yang, M. D. Rossell, P. Yu, Y. H. Chu, J. F. Scott, J. W. Ager, 3rd, L. W. Martin, R. Ramesh, Above-bandgap voltages from ferroelectric photovoltaic devices, Nat. Nanotechnol. 5 (2010) 143-147.
[24] H. Matsuo, Y. Noguchi, M. Miyayama, Gap-state engineering of visible-light-active ferroelectrics for photovoltaic applications, Nat. Commun. 8 (2017) 207.
[25] M. Wang, B. Wang, F. Huang, Z. Lin, Enabling PIEZOpotential in PIEZOelectric Semiconductors for Enhanced Catalytic Activities, Angew. Chem., Int. Ed. Engl. 58 (2019) 7526-7536.
[26] J. He, F. Gao, H. Wang, F. Liu, J. Lin, B. Wang, C. Liu, F. Huang, Z. Lin, M. Wang, C-Doped $KNbO_3$ single crystals for enhanced piezocatalytic intermediate water splitting, Environ. Sci.: Nano 9 (2022) 1952-1960.
[27] A. M. Balakt, C. P. Shaw, Q. Zhang, The decrease of depolarization temperature and the improvement of pyroelectric properties by doping Ta in lead-free $0.94Na_{0.5}Bi_{0.5}TiO_3$-$0.06BaTiO_3$ ceramics. Ceram. Int. 43 (2017) 3726-3733.
[28] S. Hao, M. Yao, G. Vitali-Derrien, P. Gemeiner, M. Otoničar, P. Ruello, H. Bouyanfif, P.-E. Janolin, B. Dkhil, C. Paillard, Optical absorption by design in a ferroelectric: co-doping in $BaTiO_3$, J. Mater. Chem. C 10 (2022) 227-234.
[29] T. Shi, G. Li, J. Zhu, Compositional design strategy for high performance ferroelectric oxides with perovskite structure, Ceram. Int. 43 (2017) 2910-2917.
[30] Y. Liu, F. Guo, B. Yang, S. Zhao, Enhanced photovoltaic effect derived from the regulation of Jahn–Teller distortion in a lattice compensation structure, Appl. Phys. Lett. 119 (2021) 233901.
[31] P. zBarone, K. Yamauchi, S. Picozzi, Jahn-Teller distortions as a novel source of multiferroicity, Phys. Rev. B 92 (2015) 014116.
[32] S. Das, S. Ghara, P. Mahadevan, A. Sundaresan, J. Gopalakrishnan, D. D. Sarma, Designing a Lower Band Gap Bulk Ferroelectric Material with a Sizable Polarization at Room Temperature, ACS Energy Lett. 3 (2018) 1176-1182.
[33] M. Shen, W. Li, M.-Y. Li, H. Liu, J. Xu, S. Qiu, G. Zhang, Z. Lu, H. Li, S. Jiang, High room-temperature pyroelectric property in lead-free BNT-BZT ferroelectric ceramics for thermal energy harvesting, J. Eur. Ceram. Soc. 39 (2019) 1810-1818.
[34] W. Liu, X. Ren, Large piezoelectric effect in Pb-free ceramics, Phys. Rev. Lett. 103 (2009) 257602.
[35] S. Yao, W. Ren, H. Ji, X. Wu, P. Shi, D. Xue, X. Ren, Z.-G. Ye, High pyroelectricity in lead-free $0.5Ba(Zr_{0.2}Ti_{0.8})O_3$-$0.5(Ba_{0.7}Ca_{0.3})TiO_3$ ceramics, J. Phys. D: Appl. Phys. 45 (2012) 195301.
[36] A. Bihari Swain, D. Murali, B. R. K. Nanda, P. Murugavel, Large Bulk Photovoltaic Response by Symmetry-Breaking Structural Transformation in Ferroelectric $[Ba(Zr_{0.2}Ti_{0.8})O_3]_{0.5}[(Ba_{0.7}Ca_{0.3})TiO_3]_{0.5}$, Phys. Rev. Appl. 11 (2019)

044007.
[37] A. B. Swain, S. D. Kumar, V. Subramanian, P. Murugavel, Influence of external electric field on the physical characteristics of lead free BZT- BCT piezoceramic. J. Alloys Compd. 787 (2019) 990-995.
[38] W. Li, Z. Xu, R. Chu, P. Fu, G. Zang, Polymorphic phase transition and piezoelectric properties of $(Ba_{1-x}Ca_x)(Ti_{0.9}Zr_{0.1})O_3$ lead-free ceramics, Phys. B: Condens. Matter 405 (2010) 4513-4516.
[39] A. Mondal, P. Saha, B. Ghosh, M. Sahu, G. D. Mukherjee, R. Ranjan, K. Brajesh, High-pressure structural investigation on lead-free piezoelectric $0.5Ba(Ti_{0.8}Zr_{0.2})O_3$-$0.5(Ba_{0.7}Ca_{0.3})TiO_3$, J. Am. Ceram. Soc. 103 (2020) 5259-5269.
[40] V. Buscaglia, S. Tripathi, V. Petkov, M. Dapiaggi, M. Deluca, A. Gajovic, Y. Ren, Average and local atomic-scale structure in $BaZr_xTi_{(1-x)}O_3$ (x = 0. 10, 0.20, 0.40) ceramics by high-energy x-ray diffraction and Raman spectroscopy, J. Phys. Condens. Matter 26 (2014) 065901.
[41] S. Miao, J. Pokorny, U. M. Pasha, O. P. Thakur, D. C. Sinclair, I. M. Reaney, Polar order and diffuse scatter in $Ba(Ti_{1-x}Zr_x)O_3$ ceramics, J. Appl. Phys. 106 (2009) 114111.
[42] N. V. Dang, T.-L. Phan, T. D. Thanh, V. D. Lam, L. V. Hong, Structural phase separation and optical and magnetic properties of $BaTi_{1-x}Mn_xO_3$ multiferroics, J. Appl. Phys. 111 (2012) 113913.
[43] M. Deluca, C. A. Vasilescu, A. C. Ianculescu, D. C. Berger, C. E. Ciomaga, L. P. Curecheriu, L. Stoleriu, A. Gajovic, L. Mitoseriu, C. Galassi, Investigation of the composition-dependent properties of $BaTi_{1-x}Zr_xO_3$ ceramics prepared by the modified Pechini method, J. Eur. Ceram. Soc. 32 (2012) 3551-3566.
[44] T. Strathdee, L. Luisman, A. Feteira, K. Reichmann, F. Morrison, Ferroelectric-to-Relaxor Crossover in (1-x)$BaTiO_3$-x$BiYbO_3$ ($0 \leq x \leq 0.08$) Ceramics, J. Am. Ceram. Soc. 94 (2011) 2292-2295.
[45] D. Zheng, H. Deng, S. Si, Y. Pan, Q. Zhang, Y. Guo, P. Yang, J. Chu, Modified structural, optical, magnetic and ferroelectric properties in (1-x)$BaTiO_3$-x$BaCo_{0.5}Nb_{0.5}O_{3-\delta}$ ceramics, Ceram, Int. 46 (2020) 6073-6078.
[46] Z. Pei, K. Leng, W. Xia, Y. Lu, H. Wu, X. Zhu, Structural characterization, dielectric, magnetic and optical properties of double perovskite Bi_2FeMnO_6 ceramics, J. Magn. Magn. Mater. 508 (2020) 166891.
[47] W. Peng, L. Li, S. Yu, P. Yang, K. Xu, Dielectric properties, microstructure and charge compensation of MnO_2-doped $BaTiO_3$-based ceramics in a reducing atmosphere, Ceram. Int. 47 (2021) 29191-29196.
[48] F. G. Wang, I. Grinberg, A. M. Rappe, Band gap engineering strategy via polarization rotation in perovskite ferroelectrics, Appl. Phys. Lett. 104 (2014) 152903.
[49] R. Inoue, S. Ishikawa, Y. Kitanaka, T. Oguchi, Y. Noguchi, M. Miyayama, Photocurrent Characteristics of Mn-Doped Barium Titanate Ferroelectric Single Crystals, Jpn. J. Appl. Phys. 52 (2013) 259-264.
[50] J. Jeong, Y. H. Han, Electrical properties of acceptor doped $BaTiO_3$, J.

Electroceram. 13 (2004) 549-553.
[51] S. Chikada, T. Kubota, A. Honda, S. I. Higai, Y. Motoyoshi, N. Wada, K. Shiratsuyu, Interactions between Mn dopant and oxygen vacancy for insulation performance of $BaTiO_3$, J. Appl. Phys. 120 (2016) 142122.
[52] H. Fang, C. Xu, J. Ding, Q. Li, J. L. Sun, J. Y. Dai, T. L. Ren, Q. Yan, Self-Powered Ultrabroadband Photodetector Monolithically Integrated on a PMN-PT Ferroelectric Single Crystal, ACS Appl. Mater. Interfaces 8 (2016) 32934-32939.
[53] F. Guo, B. Yang, S. Zhang, F. Wu, D. Liu, P. Hu, Y. Sun, D. Wang, W. Cao, Enhanced pyroelectric property in $(1-x)(Bi_{0.5}Na_{0.5})TiO_3$-$xBa(Zr_{0.055}Ti_{0.945})O_3$: Role of morphotropic phase boundary and ferroelectric-antiferroelectric phase transition, Appl. Phys. Lett. 103 (2013) 182906.
[54] Y. Bai, P. Tofel, J. Palosaari, H. Jantunen, J. Juuti, A Game Changer: A Multifunctional Perovskite Exhibiting Giant Ferroelectricity and Narrow Bandgap with Potential Application in a Truly Monolithic Multienergy Harvester or Sensor, Adv. Mater. 29 (2017) 1700767.